PAPER

Check for updates

Probing the thermal-enhanced catalytic activity of CO oxidation over Pd/OMS-2 catalysts†

Xin Liu, Qiulin Zhang, [ID]* Ping Ning,* Qixian Liu, Zhongxian Song and Yankang Duan

The present research has probed the effect of different thermal-treatment temperatures on the catalytic activity of CO oxidation and the physio-chemical properties of an OMS-2 supported palladium catalyst. The catalytic activity of Pd/OMS-2 increased with an increase in the thermal-treatment temperature from 300 to 500 °C. The optimal Pd/OMS-2 catalyst exhibited over 99% CO conversion at 35 °C. An elevated thermal-treatment temperature up to 500 °C led to a decrease in OMS-2 crystallinity and surface chemisorbed oxygen (−OH), while the surface atomic ratios of oxygen/Mn and palladium increased with the calcination temperature. A high thermal-treatment temperature above 500 °C led to the phase transformation of OMS-2 into Mn_2O_3, and an abrupt alteration in the Pd−support interaction and deactivation of the Pd/OMS-2 catalyst.

1. Introduction

Catalytic oxidation of carbon monoxide (CO) has been widely explored in the fields of low-caloric-value gas catalytic combustion, automobile exhaust purification, indoor air cleaning and academic research.[1,2] Supported Au,[3] Ag[4] and platinum group metals (PGMs)[5] have been explored and regarded as active for a low-temperature catalytic oxidation of CO approach at below room temperature. In terms of commercial application, palladium-based catalysts have been applied to CO and hydrocarbons (HC) from automobile and industrial exhausts due to their reasonable price, superior low-temperature activity and stability.[6] Multi-valence transitional and rare-earth metal oxides (oxides of Co, Mn, Fe, Ni, Cu, Ce, etc.) have been known to have oxygen vacancies, excellent oxygen storing capacity (OSC) and redox properties.[7–9] Since CO adsorption, oxygen storing and transfer capacity are critical for the low-temperature catalytic oxidation of CO over metal oxide supported palladium catalysts, there remains a substantial amount of work to optimize oxygen vacancies, OSC and the surface dispersion of palladium over multi-valence metal oxide supported palladium catalysts. Molecular sieves with ordered porosity are preferred to enhance the stability and surface dispersion of palladium, while multi-valence manganese oxides are known for their excellent OSC and redox properties. Octahedral molecular sieves (OMS-2) simultaneously contain multi-valence Mn^{2+}, Mn^{3+}, Mn^{4+} manganese oxide and the ordered 2×2 microchannels of molecular sieves.[10] However, in order to

enhance the dispersion of palladium and the redox properties of Pd/OMS-2, there remain great efforts to optimize the morphology and surface chemical properties of the OMS-2 structure. In our previous work,[11] we found that different preparation methods have an obvious effect on the crystallinity, morphology, surface chemical properties and catalytic oxidation of the Pd/OMS-2 catalysts. OMS-2 nanorods prepared by a hydrothermal method exhibit optimal catalytic properties. In recent years, a facile calcination-enhanced redispersion of palladium over metal oxide supported Pd catalysts has been reported to be active for low-temperature CO oxidation.[12,13] Despite a substantial amount of work on the thermal stability of OMS-2,[14,15] to the best of our knowledge, the thermal-enhanced catalytic activity of CO oxidation over a Pd/OMS-2 catalyst has rarely been reported.

Our interest has been attracted in exploring the effect of elevating thermal-treatment temperature on the phase composition, oxygen vacancies, surface chemical properties and catalytic activity of CO oxidation over Pd/OMS-2 catalysts.

2. Experimental

2.1 Catalyst preparation

2.1.1 Preparation of OMS-2. All OMS-2 supports are prepared with a conventional hydrothermal method, as described previously.[11] In a typical procedure, 19.3 mmol of $Mn(CH_3COO)_2 \cdot 4H_2O$, 27.8 mmol of $KMnO_4$ and 1 mL of concentrated nitric acid were added to 64 mL of distilled water with stirring. The mixture was then transferred into a Teflon-lined stainless steel autoclave and hydrothermally treated at 100 °C for 24 h. The resulting precipitate was filtered, washed with deionized water, dried at 100 °C overnight and calcined at 350 °C for 3 h with a heating rate of 3 °C min^{-1}.

Faculty of Environmental Science and Engineering, Kunming University of Science and Technology, Kunming, 650500, PR China. E-mail: qiulinzhang_kmust@163.com; ningping_58@126.com; Tel: +86-871-65170905

2.1.2 Preparation of Pd/OMS-2. Pd/OMS-2 catalysts are prepared with an impregnation method using palladium nitrate as precursor with a palladium content of 1% (wt%). The above prepared OMS-2 has been impregnated with an aqueous solution of Pd(NO$_3$)$_2$ and dried at 70 °C. The dried powders were calcined at 300, 400, 500 and 600 °C and denoted by Pd/OMS-2-300, Pd/OMS-2-400, Pd/OMS-2-500, Pd/OMS-2-600, respectively. For example, Pd/OMS-2-500 means calcining Pd(NO$_3$)$_2$ impregnated OMS-2 at 500 °C for 4 h with a heating rate of 3 °C min^{-1}.

2.2 Catalyst characterization

X-ray powder diffraction (XRD) analysis was performed on a Bruker D8 Advance diffractometer system, with an operating voltage of 40 kV and a current of 40 mA, using Cu-Kα radiation (λ = 1.5406 nm) and a graphite monochromator. The samples were investigated in the 2θ range from 10 to 70° at a scanning speed of 0.03° s^{-1}. X-ray photoelectron spectroscopy (XPS) tests were carried out on an ULVAC PHI 5000 Probe-II spectrometer using Al K$_\alpha$ radiation under UHV. The C 1s peak (284.8 eV) was used for the calibration of the binding energy values. The surface atomic concentrations of Mn, Pd, and O, as well as the peak areas were determined with the XPS Peak Fit (Version 4.0, AISN Software Inc.) software. Transmission electron microscopy (TEM) tests were measured on a FEI Tecnai G220 transmission electron microscope, using an accelerating voltage of 200 kV. N$_2$ adsorption/desorption tests were carried out on a Micromeritics TriStar II 3020 instrument at 77 K using liquid N$_2$ as adsorbent. Specific surface areas (SSAs) were determined by the Brunauer–Emmett–Teller (BET) equation. The pore volume was determined from the adsorption isotherms. Pore size distributions were determined by the non-local density functional theory (NL-DFT). The low-temperature H$_2$-temperature programmed reduction (H$_2$-TPR) tests were performed on a homemade U-shaped quartz-tube fixed-bed reactor (i.d. 3 nm). A 10 mg sample and 30 mg of quartz sand were mixed and filled for each measurement. The samples were pre-treated in flowing N$_2$ (30 mL min^{-1}) at 300 °C for 60 min and then cooled to 0 °C. After that, all H$_2$-TPR runs were performed from 0 to 90 °C under 5% H$_2$ in Ar with a heating rate of 92 °C min^{-1}. Prior to the reaction, the catalysts were pre-treated in flowing N$_2$ (30 mL min^{-1}) at 300 °C for 60 min and then cooled to 0 °C. A thermal conductivity detector (TCD) was used to monitor the online consumption of H$_2$. Raman tests were performed on a Renishaw inVia Laser micro confocal Raman spectrometer system equipped with a 50× Leica objective lense to select the target area (spot) of the sample. Laser Raman tests were carried out on the same spot irradiated by a visible Ar ion laser (514.5 nm). Prior to the test, steady-flow argon was introduced into the catalyst held at 25 °C for 30 min.

2.3 Catalytic activity test

Catalytic activity of CO oxidation was studied in a down-flow quartz-tube reactor (i.d. = 6 mm) with a K-type thermocouple enclosed to monitor the reaction temperature. 200 mg of catalyst was used for each reaction and the total gas flow rate was 50 mL min^{-1} under atmospheric pressure. The reaction gas contents consist of 1% CO (vol%) and 10.5% O$_2$ (vol%) balanced with N$_2$. The gas components were detected by a gas chromatograph with a TDX-01 column, a methanator and a flame ionization detector (FID) under steady-state conditions. The conversion of CO oxidation was calculated using the following equation:

$$CO\ conversion(\%) = \frac{[CO]_{in} - [CO]_{out}}{[CO]_{in}} \times 100$$

where [CO]$_{in}$ is the CO concentration in the feed gas and [CO]$_{out}$ is the CO concentration in the effluent gas.

3. Results and discussion

3.1 Catalytic activity

It can be seen from Fig. 1 that the conversion of CO catalytic oxidation followed the orders of: Pd/OMS-2-500 > Pd/OMS-2-400 > Pd/OMS-2-300 > Pd/OMS-2-600. Over 99% CO conversion could be obtained by Pd/OMS-2-300, Pd/OMS-2-400 and Pd/OMS-2-500 at 35 °C, approaching room temperature. It should be noted that Pd/OMS-2-500 exhibits over 96% CO conversion below 20 °C. Over 96% CO conversion could also be obtained by Pd/OMS-2-400 and Pd/OMS-2-500. Pd/OMS-2-600 attained 99% CO conversion at no more than 50 °C. The overall catalytic conversion of CO oxidation increases with the calcination temperature of the palladium impregnated OMS-2. While a high calcination temperature above 500 °C may lead to an abrupt decrease in catalytic activity. Since the concentration of O$_2$ is over 9% (v/v), much higher than the CO concentration, the reaction can be simplified to zero order with respect to oxygen and +1 with respect to CO for low CO concentration. The optimal Pd/OMS-2-500 exhibits an apparent activation energy of 12.8 kJ mol^{-1} (Fig. S1†). Therefore, it has attracted our great interest to further explore the potential reasons for this thermally-induced elevated activity and abrupt deactivation.
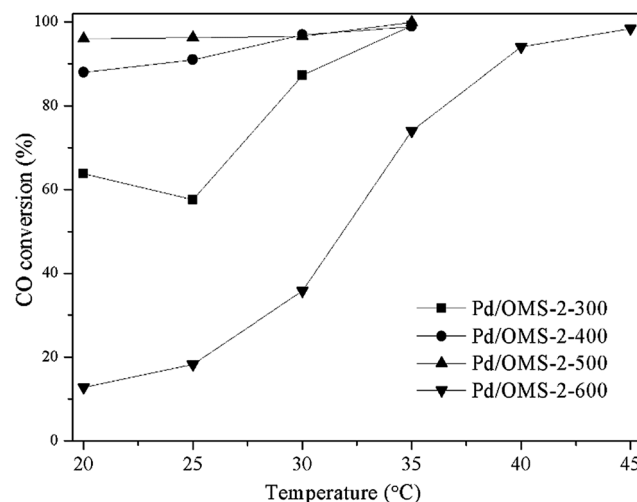

Fig. 1 Conversion of CO catalytic oxidation over various catalysts (1.0 vol% CO, 10.5 vol% O$_2$, N$_2$ balanced and GHSV of 15 000 mL g^{-1} h^{-1}).
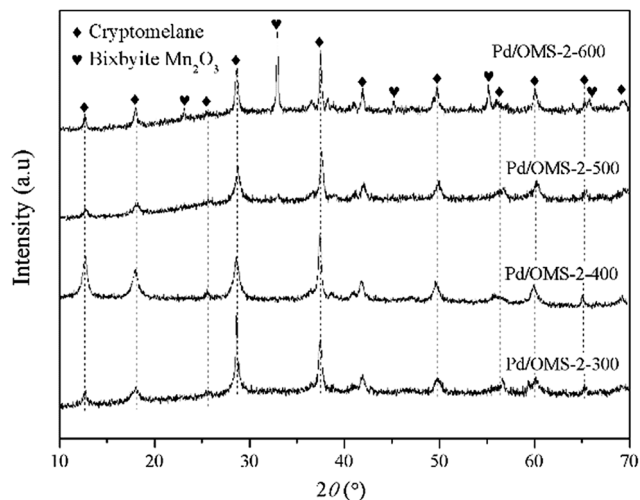
Fig. 2 X-ray diffraction (XRD) patterns of the various catalysts.

3.2 XRD analysis

X-ray diffraction (XRD) spectra of various catalysts are shown in Fig. 2. All samples show obvious diffraction peaks of crypto-melane $K_{2-x}Mn_8O_{16}$ structure (PDF# 44-1386), indicating the existence of an octahedral molecular sieve (OMS-2) structure. The intensity of the diffraction peaks decreased when the calcination temperature increased from 300 to 500 °C. Therefore, it should be concluded that a relatively high calcination temperature is preferred to decrease the crystallinity. Obvious diffraction peaks of bixbyite Mn_2O_3 (PDF# 41-1442) could also be seen from the pattern of Pd/OMS-2-600, indicating that a relatively high calcination temperature beyond 500 °C could result in the formation of highly-crystalline bixbyite Mn_2O_3 and

$K_{2-x}Mn_8O_{16}$. A potential phase transformation and sintering of the OMS-2 structure may have happened when the calcination temperature shifted from 500 to 600 °C. No obvious character-ization peaks of palladium species could be observed from any of the samples, indicating that palladium species existed in the form of highly dispersed non-crystalline species or semicrystals beyond the detection limit of XRD analysis. Overall, it could be concluded that no sintering of palladium crystals could be observed from any of the samples within the detection limits of the XRD technique. Crystallinity decreased with an elevation of the calcination temperature from 300 to 500 °C, while the catalytic activity increased with the thermal-treatment temperature.

3.3 N_2 adsorption–desorption tests

N_2 adsorption–desorption isotherms of various samples are shown in Fig. 3. Hysteresis loops of all samples starting at $P/P_0 \geq 0.75$ and terminating at P/P_0 approach 1.0, indicating the presence of interparticle spaces and an abundance of ordered micropores over OMS-2's primitive topological structure (0.46 nm of 2 × 2 microchannels). The NL-DFT pore size distributions (PSD) of various samples are listed in Fig. 4. No obvious gradual uptakes or inflection points approaching $P/P_0 = 0$ could be observed, indicating the low volumes of micropores in all the samples, despite the ordered 1-D microchannels of the OMS-2 structure. It should be noted that a majority of the OMS-2 reported previously exhibit the morphology of nano-particles or nanorods, which may facilitate the formation of interparticle space. While our present PSD results (Fig. S2†) indicate a character which is more like interparticle space than the ordered microchannels of an OMS-2 structure. However, further morphological studies of TEM and STEM are required to
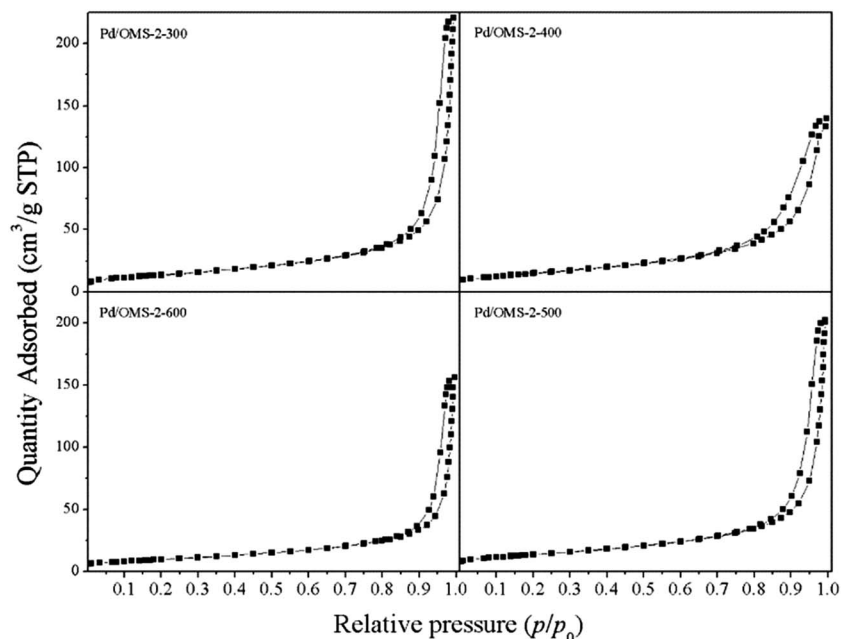

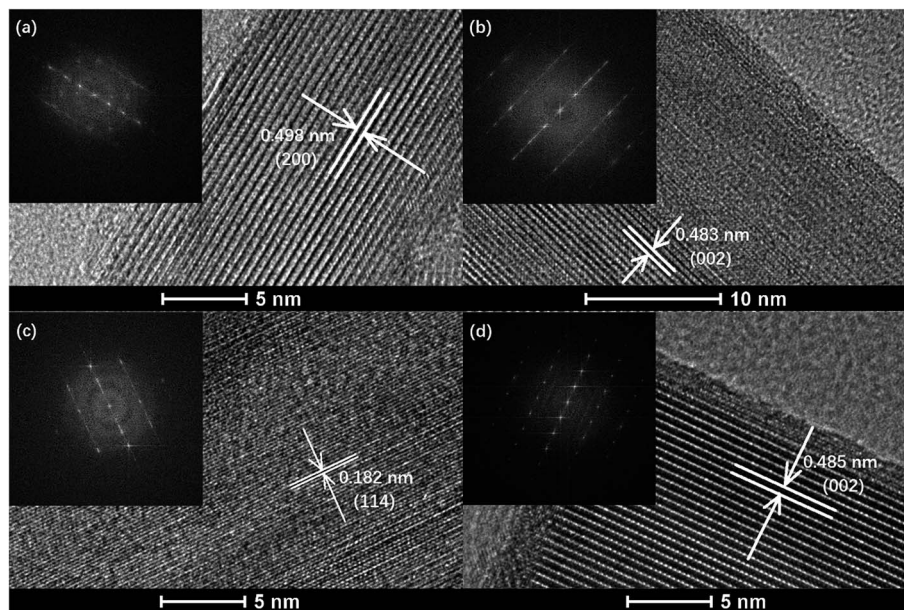Fig. 3 N_2 adsorption–desorption isotherms of various catalysts.

Fig. 4 HR-TEM images of (a) Pd/OMS-2-300, (b) Pd/OMS-2-400, (c) Pd/OMS-2-500, (d) Pd/OMS-2-600.

Table 1 Specific surface area (SSA), pore volume and average pore size of various samples

Samples	SSA^a $(m^2\ g^{-1})$	Pore volume^b $(m^3\ g^{-1})$	Average pore size^c (nm)
Pd/OMS-2-300	49.4	0.311	25.2
Pd/OMS-2-400	53.5	0.195	14.5
Pd/OMS-2-500	47.0	0.297	24.8
Pd/OMS-2-600	35.0	0.211	24.1

^{a} Specific surface area (SSA) was calculated from Brunauer–Emmett–Teller (BET) equation. ^{b} Pore volume was calculated from single point adsorption total pore volume of pores less than 189.4 nm width at $P/P_0 = 0.990000000$. ^{c} Average pore size was determined from adsorption average pore diameter ($4V/A$ by BET).

further discuss the speculation mentioned above. It can be seen from Table 1 that the specific surface areas (SSA) of different samples follow the order of: Pd/OMS-2-400 > Pd/OMS-2-300 > Pd/OMS-2-500 > Pd/OMS-2-600. The present research indicates that SSA has no significant effect on the catalytic activity of the Pd/OMS-2 catalysts.

3.4 High resolution transmission electron microscope (HR-TEM) analysis

High resolution transmission electron microscope (HR-TEM) images of various samples are shown in Fig. 4. All samples show a dispersed regular well-crystalline nanorod structure with a single or multiple crystal plane exposed. The diameter of the samples ranges from 35 to 55 nm and the length of the samples ranges from 200 to 400 nm (ESI Fig. S3 to S6†). No obvious aggregated particles of palladium species could be found, indicating high dispersion of the palladium species despite a high calcination temperature above 500 °C. A minority of semi

crystals and irregular accumulated nanoparticles could be observed from all the samples. The irregular dispersed nano-rods and accumulated nanoparticles may contribute to the interparticle space, as described in N_2 adsorption–desorption analysis (Fig. 3 and Table 1). It should be noted that Pd/OMS-2-300 and Pd/OMS-2-400 show a relatively regular well-crystalline structure with the regular shape of a long longitude nanorod (ESI Fig. S3 to S6†).

3.5 X-ray photoelectron spectroscopy (XPS) analysis

X-ray photoelectron spectroscopy (XPS) analysis was employed to analyze the chemical state and atomic concentration of surface palladium, manganese, and oxygen species. ULVAC-PHI MultiPak™ Software Manual (Version 9, ULVAC-PHI Inc.) has been utilized to analyze the surface atomic concentration. It has also been reported that surface molar ratios of oxygen vacancies (Mn^{3+}/Mn^{4+}), Mn^{n+}/Mn_{total} and $O_{adsorbed}/O_{lattice}$ have an important influence on oxygen storage and transfer capacity over multi-valence manganese oxides due to the dynamic balance of $Mn^{n+} \xleftarrow{e^-} Mn^{(n-1)+}$ and $-Mn^{4+}-O^{2-}-Mn^{4+}- \rightarrow -Mn^{3+}-O-Mn^{3+}- + 1/2O_2$ in the presence of gaseous oxygen.[16] Therefore, the present study has analyzed the surface molar ratios of Mn^{2+}/Mn_{total}, Mn^{3+}/Mn_{total}, Mn^{4+}/Mn_{total} and $O_{adsorbed}/O_{lattice}$ over the various catalysts using XPS PeakFit (Version 4.0, AISN Software Inc.) software.

The surface atomic ratios of Mn^{2+}/Mn_{total}, Mn^{3+}/Mn_{total} and Mn^{4+}/Mn_{total} were calculated as follows:

$$Mn^{2+}/Mn_{total} = \frac{S_1}{S_1 + S_2 + S_3}$$

$$Mn^{3+}/Mn_{total} = \frac{S_1}{S_1 + S_2 + S_3}$$

$$\text{Mn}^{4+}/\text{Mn}_{\text{total}} = \frac{S_1}{S_1 + S_2 + S_3}$$

where S_1, S_2 and S_3 represent the corresponding peak areas of Mn^{2+}, Mn^{3+} and Mn^{4+}, respectively.

The surface atomic ratios of $\text{O}_{\text{adsorbed}}/\text{O}_{\text{lattice}}$ were calculated using the following equation:

$$\text{O}_{\text{adsorbed}}/\text{O}_{\text{total}} = \frac{S_{\text{adsorbed}}}{S_{\text{adsorbed}} + S_{\text{lattice}}}$$

where S_{adsorbed} and S_{lattice} are the peak areas corresponding to O^{2-} and $\text{OH}^-/\text{CO}_3^{2-}$, respectively.

It can be seen from Fig. 5 that Pd $3d_{5/2}$ and Pd $3d_{3/2}$ peaks located at 337.32 ± 0.04 eV and 342.65 ± 0.04 eV, respectively, indicate the existence of the Pd(II) state.[17,18] No characteristics of Pd(IV) species could be observed from the peaks of the Pd 3d spectrum.[19] It should also be noted that the present XPS technique has insufficient evidence to confirm the existence of strong metal–support interacted Pd(II) (Pd$_{\text{SMSI}}$). XPS spectra of Mn 2p in Fig. 6 showed 2p peaks of Mn located at 640.90 ± 0.04 eV, 642.10 ± 0.04 eV and 643.50 ± 0.04 eV indicating that Mn species coexisted in the multi-valence states of Mn^{2+}, Mn^{3+} and Mn^{4+}.[20,21] The O 1s XPS spectra of the catalysts can be resolved into two peaks, as shown in Fig. 7. The peaks at 529.76 ± 0.03 eV (denoted by $\text{O}_{\text{lattice}}$) could be attributed to the characteristic peak of metal–oxygen (the lattice oxygen, O^{2-}), while the peaks at 531.5 eV (denoted by $\text{O}_{\text{adsorbed}}$) are generally regarded as the surface chemisorbed oxygen (OH^- or CO_3^{2-}).[22,23]

Surface $\text{Mn}^{2+} : \text{Mn}^{3+} : \text{Mn}^{4+}$ molar ratios of all samples are listed in Table 2. No obviously different molar ratios of $\text{Mn}^{2+} : \text{Mn}^{3+} : \text{Mn}^{4+}$ could be observed from Pd/OMS-2-300, Pd/OMS-2-400 or Pd/OMS-2-500, indicating the maintenance of the OMS-2 structure.[20] Rare surface potassium (K^+) could be seen from Pd/OMS-2-300 and Pd/OMS-2-400, indicating the occupation of K^+ in the 2×2 microchannels of the OMS-2 structure. However, Pd/OMS-2-500, Pd/OMS-2-600 showed a sudden emergence of surface potassium (K^+). In addition,
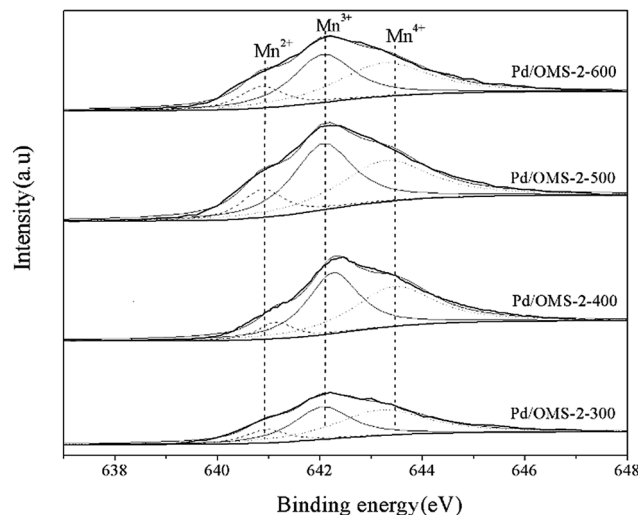

Fig. 6 XPS spectra of Mn 2p over various samples.

surface atomic ratios of palladium increased with the elevation of the thermal-treatment temperature above 400 °C. There was a potential spill-over effect of K^+ from the 2×2 microchannels and/or decomposition of strong metal–support interacted palladium (Pd$_{\text{SMSI}}$) during the thermal treatment process at 500 to 600 °C. Above all, it could be concluded that an increase in thermal treatment temperature from 300 to 500 °C is preferred to improve surface palladium and potassium species, while the catalytic activity of CO oxidation also increased with the elevation of the calcination temperature from 300 to 500 °C.

It could be observed from Table 2 that Pd/OMS-2-400 and Pd/OMS-2-500 show approximately $2 : 1$ surface O/Mn atomic ratios, while the surface O/Mn atomic ratios Pd/OMS-2-300 and Pd/OMS-2-600 are 3.48 and 2.58, respectively, which are obviously higher than the stoichiometric ratio of $\text{K}_{2-x}\text{Mn}_8\text{O}_{16}$. Is known that a majority of surface hydroxyl groups ($-\text{OH}$) may contribute to an increase in surface oxygen of the OMS-2 structure. While it is also known that a higher thermal treatment temperature may
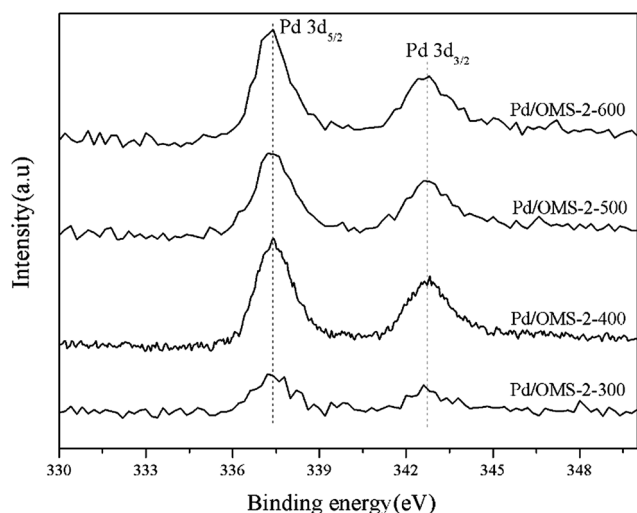

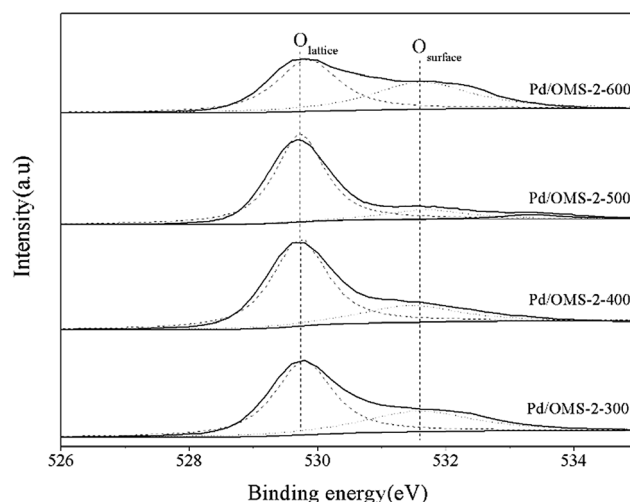**Fig. 5** XPS spectra of Pd 3d over various samples.

Fig. 7 XPS spectra of O 1s over various samples.

Table 2 Surface atomic ratios of Mn^{2+}/Mn_{total}, Mn^{3+}/Mn_{total}, Mn^{4+}/Mn_{total}, $O_{adsorbed}/O_{lattice}$ and surface atomic concentrations (%) of various samples

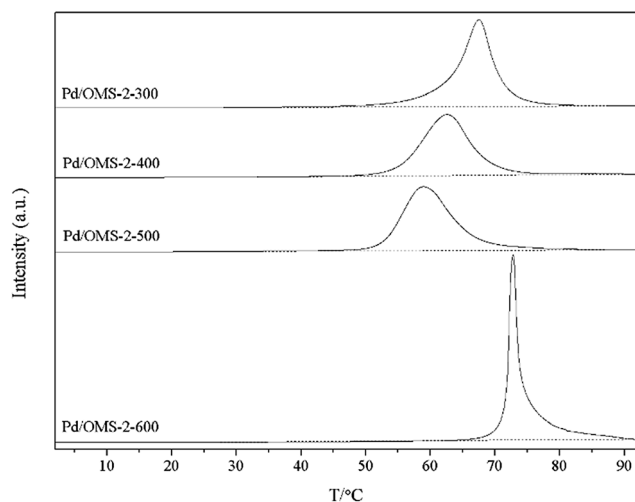| Samples | Surface atomic concentration (%) | | | | $\dfrac{O_{adsorbed}}{O_{total}}$ | $\dfrac{Mn^{2+}}{Mn_{total}}$ | $\dfrac{Mn^{3+}}{Mn_{total}}$ | $\dfrac{Mn^{4+}}{Mn_{total}}$ |
	Pd	O	Mn	K				
Pd/OMS-2-300	0.34	77.40	22.26	0.00	43.38	30.89	34.09	35.02
Pd/OMS-2-400	0.50	66.00	33.50	0.00	40.07	29.68	35.23	35.08
Pd/OMS-2-500	0.59	66.15	30.38	2.88	35.53	30.73	34.99	34.28
Pd/OMS-2-600	0.91	69.41	26.86	2.82	47.95	31.04	34.44	34.52

Fig. 8 Low-temperature H_2-TPR profiles of the various samples.

lead to a decrease in surface hydroxyl groups (−OH) of metal oxide.[22] Therefore, it could be speculated that surface –OH contributed to the nonstoichiometric O/Mn atomic ratios of Pd/OMS-2-300. It should be noted that our XRD analysis (Fig. 2) indicates that Pd/OMS-2-600 exhibits two major crystalline phases of Mn_2O_3 and $K_{2-x}Mn_8O_{16}$, which indicate a total stoichiometric O/Mn ratio of less than 2.0. However, as a matter of fact, Pd/OMS-2-600 shows a surface O/Mn ratio of 2.58. Therefore, further analysis of structural and chemical data (Raman and H_2-TPR. *etc.*) are expected. Although it is too early to conclude a defined correlation of catalytic activity between $O_{adsorbed}/O_{lattice}$, O/Mn atomic ratios and catalytic activity of CO oxidation, to our great interest, Pd/OMS-2-400 and Pd/OMS-2-500 exhibit approximately 2 : 1 surface O/Mn atomic ratios of OMS-2 and an obviously higher catalytic activity than Pd/OMS-2-300 or Pd/OMS-2-600. Further exploration of the redox properties (H_2-TPR) and laser Raman are expected.

3.6 H_2 temperature programmed reduction analysis (H_2-TPR)

Low-temperature programmed reduction (low-temperature H_2-TPR) has been carried out to explore the redox properties of surface palladium species under elevated temperatures in H_2/Ar. It can be seen from Fig. 8 that all samples show obvious peaks of H_2 consumption at 65 to 75 °C, indicating the

reduction of PdO and the Pd-assisted reduction of surface MnO_x-interacted Pd(II).[11,23] Peaks of reduction temperature (Fig. 8) shifted in the order Pd/OMS-2-600 (72.8 °C) > Pd/OMS-2-300 (67.5 °C) > Pd/OMS-2-400 (62.6 °C) > Pd/OMS-2-500 (58.9 °C). No significant differences in peak areas could be observed from any of the samples, indicating the same amount of H_2 consumed by Pd(II) and Pd(II) interacted surface MnO_x species (for example, Pd-O–Mn structure) (Table 3). Pd/OMS-2-300 (67.5 °C), Pd/OMS-2-400 and Pd/OMS-2-500 show relatively flat peaks with a wide full width at half maximum (FWHMs), while Pd/OMS-2-600 shows a sharp increase in peak height and a sharp decrease in full wave at half maximum (FWHM). Above all, compared with other samples, profiles of Pd/OMS-2-600 imply an abrupt alteration in the Pd–support interaction. It is reported that a relatively high calcination temperature may lead to a decrease in the strong palladium–support interaction or the transformation of Pd_{SMSI} into dispersed surface PdO and Pd^0,[12] which could enhance the low-temperature catalytic activity of CO oxidation.[24,25] Reduction of the co-existing surface Pd_{SMSI} and PdO could be regarded as a potential reason for the broader FWHMs[26] over Pd/OMS-2-300, Pd/OMS-2-400 and Pd/OMS-2-500. Combined with our XRD (Fig. 2) and HR-TEM analysis (Fig. 4), no obvious sintering of the palladium particles could be observed from the Pd/OMS-2-600, due to the low content of palladium. However, sintering of the OMS-2 structure, phase transformation and changes in surface chemical properties (for example, the spill-over of Pd from the 2 × 2 tunnels to the surface) at 600 °C are also potential reasons for the deactivation of Pd/OMS-2-600. In conclusion, an elevated calcination temperature from 300 to 500 °C is preferred to enhance the redox activity of palladium species, while a higher calcination temperature above 600 °C may weaken the palladium–support interaction. While it is hard to determine the key factors for the enhanced activity of Pd/OMS-2-500 and deactivation of Pd/OMS-2-600 from H_2-TPR and XPS analysis.

Table 3 Peak positions and areas of H_2 consumption over various samples

Samples	Peak position (°C)	Area
Pd/OMS-2-300	67.5	1081
Pd/OMS-2-400	62.6	1074
Pd/OMS-2-500	58.9	1075
Pd/OMS-2-600	72.8	999

3.7 Raman analysis

Confocal micro-spectroscopy Raman spectra are employed to provide complementary structural information of XRD analysis over various Pd/OMS-2 catalysts. Optical microscope images of various samples are shown in Fig. S7(a), S8(a), S9(a), S10(a) (ESI†). Raman spectra of selected spots1 (Fig. S7(a), S8(a), S9(a), S10(a) (ESI†)) exhibit well-crystalline structure. Distinct peaks of all samples at 636 to 656 cm^{-1} assignable to the symmetric vibrations of the A_{1g} stretching mode of the lattice Mn–O, indicate the existence of an octahedral MnO_6 structure with 2×2 tunnels.[14,15] It is hard to give qualitative and quantitative analysis results of surface PdO from the present Raman analysis as the influence of the Mn–O A_{1g} mode at 636 to 656 cm^{-1} approaches the distinctive Raman mode of PdO.[27,32] Bands in the region 455–569 cm^{-1} could be attributed to the asymmetric stretching of bridge oxygen species (Mn–O–Mn), indicating the existence of surface amorphous or semi-crystalline Mn_xO_y species (where $1 < x < 2$, $1 < y < 3$ and $1 < y/x < 1.5$).[28] It can be seen from Fig. 9(a) that the peak of Pd/OMS-2-600 at 348 cm^{-1} is the out-of-plane bending mode of Mn_2O_3, indicating the presence of Mn_2O_3.[29] Bands of Pd/OMS-2-300 and Pd/OMS-2-400 at 182 cm^{-1} indicate the presence of an Mn–O–M metal–oxygen chain interacting with the occupation of K^+ in the 2×2 tunnels.[30,31]

Shoulders at 578 cm^{-1} corresponding to the symmetric vibrations of the F_{2g} mode of the lattice Mn–O could be observed from Pd/OMS-2-300 and Pd/OMS-2-400 (Fig. 9(a)),[14] indicating the existence of the well-developed tetragonal structure of MnO_6 octahedral chains with K^+ occupied inside the 2×2 tunnels.[32,33] This slight F_{2g} mode of the lattice Mn–O peak could not be observed from the spectra of Pd/OMS-2-500 or Pd/OMS-2-600. Moreover, bands of Pd/OMS-2-300 and Pd/OMS-2-400 at 182 cm^{-1} and 578 cm^{-1} corresponding to the K^+ interacted

Mn–O species could not be observed from Pd/OMS-2-300 or Pd/OMS-2-400 after heating. Combined with our XPS analysis (Table 2), it is also inferred that Pd/OMS-2-500 and Pd/OMS-2-600 exhibit an abrupt increase in surface potassium and palladium, *i.e.* a spill-over of palladium and K^+ from the octahedral MnO_6-interacted 2×2 tunnels, when Pd/OMS-2 was calcined above 400 °C. It should be noted that Pd/OMS-2-500 exhibits no obvious shifts and the peaks disappear before and after being heated at 450 °C in Ar. In other words, compared with Pd/OMS-2-300 and Pd/OMS-2-400, Pd/OMS-2-500 exhibits a higher thermal stability.

4. Discussion

The gradual evolution of surface species and metal–support interactions with the different thermal-treatment temperatures have been characterized by XPS H_2-TPR and Raman analysis. Reduction peaks of H_2-TPR over the samples shifted to a lower temperature as the thermal-treatment temperature increased from 300 to 500 °C. An elevated calcination temperature up to 500 °C is the potential influencing factor for decreasing palladium (or potassium)–support interaction. Raman analysis indicated the decrease (or disappearance) of bands at 182 cm^{-1} and 578 cm^{-1} corresponding to the occupation of K^+ in the 2×2 tunnels. XPS indicated no obvious proofs of Pd_{SMSI} and the differences in surface palladium (and potassium) atomic ratios over all the samples. However, all the samples exhibit the same peak areas of H_2-TPR, indicating that all samples have the same content of H_2-activated Pd(II) (Table 3). Above all, it could be speculated that the spill-over of potassium and palladium from the tunnels to the outer surface happened with the elevation in calcination temperature from 300 to 500 °C. Despite the same content of total palladium and H_2-activated Pd(II), the increase
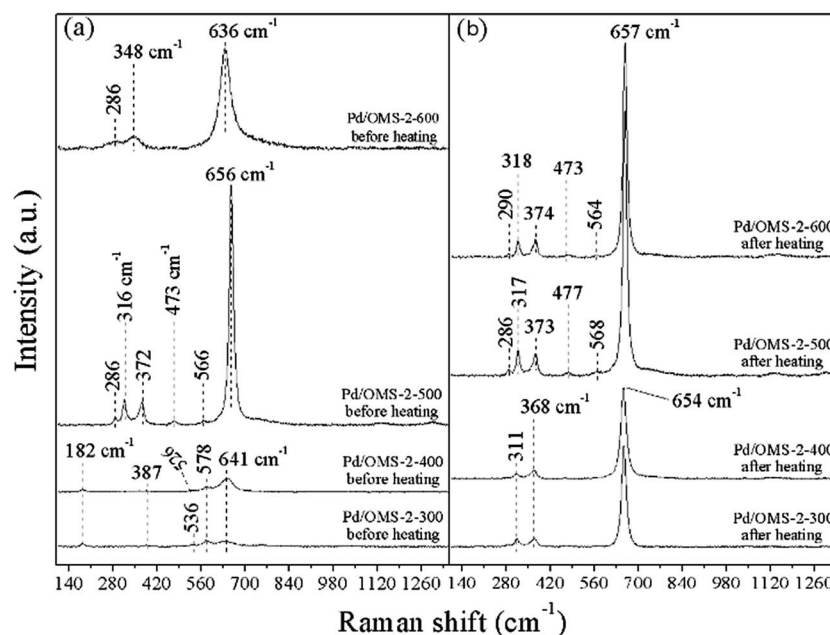

Fig. 9 Raman spectroscopy of various samples (a) before heating (room temperature), (b) cooled to room temperature after being heated at 450 °C (testing conditions: in Ar atmosphere).

in surface Pd species (proved by XPS analysis) is generally regarded as a key factor in improving CO catalytic oxidation.[12,24,25] Combined with the XPS, XRD and H_2-TPR analysis, an abrupt increase in surface oxygen and palladium, the phase transformation of $K_{2-x}Mn_8O_{16} \rightarrow Mn_2O_3$, as well as an alteration in palladium–support interactions happened when the calcination temperature shifted from 500 to 600 °C. Despite the increase in surface palladium at a thermal-treatment temperature of 600 °C, the sintering effect plays a key role in the deactivation over Pd/OMS-2-600. But it is beyond the scope of the present research to probe the detailed sintering effects on the deactivation of Pd/OMS-2-600 catalysts. Previous research on the catalytic oxidation of CO over manganese oxides and manganese oxides supported noble-metal catalysts has been listed in Table S1 in ESI.†

5. Conclusions

The present research has explored a facile thermal treating process on the catalytic activity of CO oxidation over OMS-2 supported palladium catalysts. A relatively high calcination temperature up to 500 °C is preferred to improve surface palladium atomic ratios and catalytic activity of the Pd/OMS-2 catalyst. In addition, an elevated calcination temperature up to 500 °C led to a decrease in surface $O_{adsorbed}$ and palladium (or potassium)-support interaction. Spill-over of potassium and palladium happened when the calcination temperature shifted from 400 to 500 °C. A higher calcination temperature above 500 °C may lead to the abrupt alteration of palladium–support interactions and a decrease in the catalytic activity. Phase transformation of $K_{2-x}Mn_8O_{16} \rightarrow Mn_2O_3$ happened as well. The present research indicates that an optimal thermal-treatment temperature (500 °C) existed which was attributed to the optimal surface physiochemical properties of Pd/OMS-2-500 and complete CO conversion at 35 °C.

Conflicts of interest

There are no conflicts to declare.

Acknowledgements

References

1 R. Prasad and P. Singh, *Catal. Rev.*, 2012, **54**(2), 224–279.

2 B. Min and C. FrLiuiend, *Chem. Rev.*, 2007, **107**(6), 2709–2724.

3 T. Takei, T. Akita, I. Nakamura, T. Fujitani, M. Okumura, K. Okazaki, J. Huang, T. Ishida and M. Haruta, *Adv. Catal.*, 2012, **55**, 1–126.

4 X. Zhang, Z. Qu, F. Yu and Y. Wang, *Chin. J. Catal.*, 2013, **34**(7), 1277–1290.

5 T. Nguyen, F. Morfin, M. Aouine, F. Bosselet, J. Rousset and L. Piccolo, *Catal. Today*, 2015, **253**, 106–114.

6 C. Wang, A. J. Binder, T. J. Toops, J. Lauterbach and E. Sasmaz, *Emiss. Control Sci. Technol.*, 2017, **3**, 37–46.

7 S. Kato, R. Fujimaki, M. Ogasawara, T. Wakabayashi, Y. Nakahara and S. Nakata, *Appl. Catal., B*, 2009, **89**, 183–188.

8 S. Wang, N. Li, L. Luo, W. Huang, Z. Pu, Y. Wang, G. Hu, M. Luo and J. Lu, *Appl. Catal., B*, 2014, **144**, 325–332.

9 C. Zhang, C. Wang, W. Zhan, Y. Guo, Y. Guo, G. Lu, A. Baylet and A. Giroir-Fendler, *Appl. Catal., B*, 2013, **129**, 509–516.

10 X. Chen, Y. Shen, S. Suib and C. Young, *Chem. Mater.*, 2002, **14**, 940–948.

11 Q. Zhang, Q. Liu, P. Ning, X. Liu, L. Xu, Z. Song, Y. Duan and T. Zhang, *Res. Chem. Intermed.*, 2017, **43**(4), 2017–2032.

12 S. Hinokuma, H. Fujii, M. Okamoto, K. Ikeue and M. Machida, *Chem. Mater.*, 2010, **22**, 6183–6190.

13 S. Hinokuma, H. Fujii, Y. Katsuhara, K. Ikeue and M. Machida, *Catal. Sci. Technol.*, 2014, **4**, 2990–2996.

14 C. Calvert, R. Joesten, K. Ngala, J. Villegas, A. Morey, X. Shen and S. L. Suib, *Chem. Mater.*, 2008, **20**, 6382–6388.

15 S. Dharmarathna, C. K. King'ondu, W. Pedrick, L. Pahalagedara and S. L. Suib, *Chem. Mater.*, 2012, **24**(4), 705–712.

16 J. Hou, Y. Li, L. Liu, L. Ren and X. Zhao, *J. Mate. Chem. A*, 2013, **1**(23), 6736–6741.

17 K. Priolkar, P. Bera, P. Sarode, M. Hegde, S. Emura, R. Kumashiro and N. P. Lalla, *Chem. Mater.*, 2002, **14**, 2120–2128.

18 S. Sharma, B. Devu Mukri and M. S. Hegde, *Dalton Trans.*, 2011, **40**, 11480–11489.

19 Y. Zhou, X. Liu, Q. Zhang, Q. Liu, Z. Song and P. Ning, *Res. Chem. Intermed.*, 2017, **43**(22), 1–19.

20 X. Meng, J. Zhang, B. Chen, Z. Jing and P. Zhao, *Catal. Sci. Technol.*, 2016, **6**, 890–896.

21 E. S. Ilton, J. E. Post, P. J. Heaney, F. T. Ling and S. N. Kerisit, *Appl. Surf. Sci.*, 2016, **366**, 475–485.

22 Q. Zhang, X. Liu, P. Ning, Z. Song, H. Li and J. Gu, *Catal. Sci. Technol.*, 2015, **5**, 2260–2269.

23 X. Liu, P. Ning, L. Xu, Q. Liu, Z. Song and Q. Zhang, *RSC Adv.*, 2016, **6**, 41181–41188.

24 A. I. Boronin, E. M. Slavinskaya, I. G. Danilova, R. V. Gulyaev, Y. I. Amosov, P. A. Kuznetsov, I. A. Polukhina, S. V. Koscheev, V. I. Zaikovskii and A. S. Noskov, *Catal. Today*, 2009, **144**, 201–211.

25 E. M. Slavinskaya, R. V. Gulyaev, A. V. Zadesenets, O. A. Stonkus, V. I. Zaikovskii, Y. V. Shubin, S. V. Korenev and A. I. Boronin, *Appl. Catal., B*, 2015, **91**, 166–167.

26 L. Meng, A. P. Jia, J. Q. Lu, L. F. Luo, W. X. Huang and M. F. Luo, *J. Phys. Chem. C*, 2011, **115**(40), 19789–19796.

27 A. Baylet, P. Marécot, D. Duprez, P. Castellazzi, G. Groppi and P. Forzatti, *Phys. Chem. Chem. Phys.*, 2011, **13**, 4607–4613.

28 J. Xu, Y. Deng, X. Zhang, Y. Luo, W. Mao, X. Yang, L. Ouyang, P. Tian and Y. Han, *ACS Catal.*, 2014, **4**, 4106–4115.

29 J. Xu, Y. Deng, Y. Luo, W. Mao, X. Yang and Y. Han, *J. Catal.*, 2013, **300**, 225–234.

30 C. Wang, J. Ma, F. Liu, H. He and R. Zhang, *J. Phys. Chem. C*, 2015, **119**, 23119–23126.

31 S. Cheng, L. Yang, D. Chen, X. Ji, Z. Jiang, D. Ding and M. Liu, *Nano Energy*, 2014, **9**, 161–167.

32 L. Liu, Y. Song, Z. Fu, Q. Ye, S. Cheng, T. Kang and H. Dai, *Appl. Surf. Sci.*, 2017, **396**, 599–608.

33 R. Wang and J. Li, *Environ. Sci. Technol.*, 2010, **44**, 4282–4287.